Nano Energy 96 (2022) 107117

Contents lists available at ScienceDirect

Nano Energy

journal homepage: www.elsevier.com/locate/nanoen

N-doped graphene quantum dots as charge-transfer-bridge at LaSrCoO/$MoSe_2$ heterointerfaces for enhanced water splitting

Chen Tian Cao [a,1], Sun-Woo Kim [a,1], Hee Jun Kim [a], Rahul Purbia [a], Sang Heon Kim [a], Dokyoung Kim [b,c], Kyoung Jin Choi [d], Hyesung Park [d,*], Jeong Min Baik [a,e,**]

[a] School of Advanced Materials Science and Engineering, Sungkyunkwan University (SKKU), Suwon 16419, Republic of Korea
[b] Department of Biomedical Science, Graduate School, Kyung Hee University, Seoul 02447, Republic of Korea
[c] Medical Research Center for Bioreaction to Reactive Oxygen Species and Biomedical Science Institute, School of Medicine, Kyung Hee University, Seoul 02447, Republic of Korea
[d] Department of Materials Science, Ulsan National Institute of Science and Technology (UNIST), Ulsan 44919, Republic of Korea
[e] KIST-SKKU Carbon-Neutral Research Center, Sungkyunkwan University (SKKU), Suwon 16419, Republic of Korea

ARTICLE INFO

Keywords:
Bifunctional electrocatalyst
Perovskite
$MoSe_2$
Interfacial band alignment engineering
N-doped graphene quantum dots

ABSTRACT

A bifunctional electrocatalyst interface requires superior charge transfer and good electrical conductivity to produce a water splitting reaction that is overall efficient and stable. In the context of engineering the interfacial band alignment, we demonstrate a novel and straightforward approach to control the electrochemical activity of the bifunctional catalysts with precision by bridging conductive N-doped graphene quantum dots (N-GQDs, 2–3 nm) between $La_{0.5}Sr_{0.5}CoO_{3-\delta}$ (LSC) and $MoSe_2$ interfaces. The N-GQDs govern the charge transfer process at the interface, exhibiting higher Co^{3+} cations and metallic 1 T-$MoSe_2$ phase-transition compared to those of LSC and LSC-$MoSe_2$ composites. As a result, the optimized LSC-N-GQDs-$MoSe_2$ electrocatalyst possessed a lower overpotential, Tafel slope, and charge transfer resistance in HER and OER than pure and LSC-$MoSe_2$ electrocatalysts in an alkaline solution. The Tafel slopes (64 mV·dec^{-1} and 51 mV·dec^{-1} for HER and OER respectively) are smaller than those of current solutions that are commercially available, showing a higher performance at a high current density of 500 mA·cm^{-2} with a long-term 24 h stability test. The key design of the current study is based on conductive bridging in the bifunctional catalyst to improve the interfacial charge transfer and electrochemical reaction.

1. Introduction

An affordable and practical strategy to achieve zero-carbon emissions by 2050 includes the use of hydrogen as a central strategy to reach emission goals and limit global warming to 1.5 degrees Celsius [1,2]. Hydrogen is one of the cleanest and most sustainable energy sources to generate electricity, and it is an essential counterpart to other forms of renewable generation by providing the means to store energy and overcome the intermittency to balance differences in supply and demand patterns [3–5]. There is also growing interest in clean hydrogen as a long-term, scalable, and cost-effective option for deep decarbonization in various industries, including steelmaking, maritime transport and infrastructure, aviation, and ammonia production [6–9]. There are different sources and methods to produce hydrogen for use as a fuel, and the "power-to-gas" method is commonly used to produce hydrogen at a commercial scale by splitting water with electricity on the surface of catalysts [10,11]. The "power-to-gas" method can function without creating carbon emissions by drawing electricity from renewable energy sources [12–15].

The biggest challenge to produce green hydrogen via water electrolysis is that a vast amount of power is required [16,17]. The IEA estimates that meeting today's hydrogen demand through water electrolysis would require drawing 3,600 TWh a year [18]. Thus, the power consumption of large scale hydrogen production should be

* Correspondence to: Department of Materials Science and Engineering, Ulsan National Institute of Science and Technology (UNIST), Ulsan 44919, Republic of Korea.
** Corresponding author.
E-mail addresses: hspark@unist.ac.kr (H. Park), jbaik97@skku.edu (J.M. Baik).
[1] C.T.C and S.W.K contributed equally to this work.

https://doi.org/10.1016/j.nanoen.2022.107117
Received 14 December 2021; Received in revised form 18 February 2022; Accepted 3 March 2022
Available online 6 March 2022

reduced by applying a strict systems criteria that includes a low overpotential and long-term durability at high current density. Despite tremendous efforts to find more efficient electrocatalysts to produce hydrogen, the most efficient catalysts that improve overall performance of the water electrolysis use noble metals, such as Pt, for the hydrogen evolution reaction (HER) and Ru/Ir for the oxygen evolution reaction (OER) [19–22]. However, noble metals have inherent problems when used in catalysts in that there are limited reserves, offer poor stability, and incur high costs [23,24]. Inexpensive materials with sufficiently high activity and stability have been the subject of substantial research devoted to the use of non-precious metal electrocatalysts including alloys, oxides, (oxy)hydroxides, perovskite oxides, metal sulfides, phosphides, selenides, metal pnictides, and metal-organic frameworks (MOFs) [25–32]. Recent attempts to improve the overall performance of the water electrolysis have extensively explored generating hydrogen using bifunctional catalysts in both the cathode and anode reactions in the same electrolyte. Bifunctional catalysts, such as MoC/Mo_2C [33], Fe/Ni$(OH)_2$ [34], Cu-Ni_3S_2/Co_3S_4 [35], Cu_3P @ N/P-co-doped carbon shell [36], $CoMn_2O_4$ [37], have shown clear advantages in terms of their tolerance for a wide pH range, low overpotential with a high current density, long-term stability, and simple, cost-effective preparation.

Among possible candidates for use as bifunctional catalysts, perovskite-based electrocatalysts in the form of ABO_3 (A: rare-earth or alkaline earth element, B: transition metal ion) have received significant attention owing to their low cost, abundance in nature, rich redox properties, strong catalytic activity, robust stability, compositional flexibility, and promising experimental results [28]. Among them, $La_{0.5}Sr_{0.5}CoO_{3-\delta}$ (LSC) has been extensively studied for its strong catalytic activity, unity of the e_g electron, and stronger covalent interactions between the transition metal and O atoms [38,39]. However, the materials showed a poor performance in HER catalysis due to the poor energy of hydrogen absorption [40]. To address such issues, transition metal dichalcogenides (TMDs), such as molybdenum diselenide ($MoSe_2$), were added to synthesize LSC-TMD composites that successfully achieved efficient OER and HER because the TMDs could adsorb hydrogen with a close-to-zero free energy change with a high chemical stability under alkaline conditions. The charge interplay between the LSC and $MoSe_2$ could further modify the overall physicochemical and electronic structures to favor electron transfer at the LSC/$MoSe_2$ interface [41]. Therefore, a different perspective toward catalyst design is needed to effectively modulate the electronic characteristics of catalysts with a LSC/$MoSe_2$ heterostructure in order to improve the charge conductivity and maximize the water splitting efficiency. In general, the heterostructure of such materials shows excellent performance due to the synergistic effects, an electronic interaction, and even strain effects from the unique interface structure. In addition, the high conductivity accelerates electron transmission at the interface and thus further improves the catalytic performance [42]. Thus, it is widely believed that a strongly-coupled conductive interface between LSC/$MoSe_2$ could benefit the electrocatalysis due to modulation in the electronic structure of the composite [43].

Graphene quantum dots (GQDs) are among various newly-developed materials and have drawn significant interest due to their intriguing combination of properties derived from the graphene structure and quantum-scale effects [44,45]. Interestingly, a heteroatom can be introduced in the framework of the carbon materials as an effective and versatile strategy to modify the structural and electronic properties to enhance the overall electrocatalytic performance [46]. Among various reports on heteroatom doping, nitrogen-doped carbon materials have been widely proposed as an effective way to obtain improved conductive properties [47]. Inspired by these attractive properties of N-GQDs, we hypothesize that the bifunctional activity of LSC/$MoSe_2$ heterostructures can improve through the supply of better electrochemical paths and reaction sites with a high electrical conductivity if they are well connected with conductive N-GQDs.

Here, based on the above assumption, we report on a bifunctional catalyst comprised of a perovskite oxide (LSC) and molybdenum diselenide ($MoSe_2$) heterostructure with N-doped graphene dots (N-GQDs) to achieve efficient water electrolysis by engineering the interfacial band alignment. The proposed catalyst shows excellent overall properties for water electrolysis due to synergistic effects and effective electron transport of the reaction species in distinct nanoscale regions. The HER overpotential observed for the best catalyst (in an alkaline medium) is 409 mV at current densities of 10 mA·$cm^{-2,}$ and the Tafel slope is 64 mV·dec^{-1}. For OER, the composite catalyst shows an overpotential of 302 mV at a current density of 10 mA·cm^{-2}, and the Tafel slope is 51 mV·dec^{-1}. In the 24 h stability test, LSC-N-GQDs-$MoSe_2$ keeps a cell voltage of 1.57 and 2.47 V at a current density of 10 mA·cm^{-2} and 500 mA·cm^{-2}, respectively.

The excellent catalytic performance is attributed to a close interaction between the LSC, N-GQDs, and the $MoSe_2$ nanoscale interface, ensuring effective electron transport in the composite catalyst. The superior charge transfer from LSC to $MoSe_2$ through the N-GQDs interface modulates the electronic configuration via higher Co^{3+} cations and metallic (1 T) $MoSe_2$ phase-transition as active sites, remarkably boosting the intrinsic OER and HER activity of the bifunctional catalyst. The above results are investigated in detail to understand the conductive bridge (N-GQDs) between the dual heterointerfaces (LSC and $MoSe_2$) in terms of the overall water splitting performance, which provides powerful guidance to design multi-component electrocatalysts that provide a high efficiency.

2. Experimental section

2.1. Materials

$La(NO_3)_3{\cdot}6H_2O$, $SrCl_2{\cdot}6H_2O$, $Co(NO_3)_2{\cdot}6H_2O$, Critic Acid, HNO_3 solution, Ethyl alcohol anhydrous (ethanol, 99.5%), Ethylene glycol anhydrous (99.8%), Dopamine hydrochloride, KOH (45%) solution and Hydrochloric acid (35.0–37.0%) were purchased from Sigma-Aldrich. $MoSe_2$ (~325 mesh powder, purity >99.9%) was purchased from Alfa Aesar. Deionized water was used from our laboratory, and it had an electrical resistivity of 18.2 Ω·m.

2.2. Synthesis of the LSC

$La_{0.5}Sr_{0.5}CoO_{3-\delta}$ (LSC) perovskite oxides were synthesized via a sol-gel process. Stoichiometric amounts of $La(NO_3)_3{\cdot}6H_2O$, $SrCl_2{\cdot}6H_2O$, $Co(NO_3)_2{\cdot}6H_2O$ and critic acid were mixed with 1 ml HNO_3 in a three-necked flask with stirring. After the precursors were mixed well, 15 ml ethylene glycol were added into the mixture drop by drop, with heating until the mixture achieved a state of gel. Next, the gel was washed three times with ethylene glycol via centrifugation at 13,000 rpm for 5 mins. Then, the resulting mixture was calcined at 700 °C for 12 h in ambient atmosphere.

2.3. Synthesis of N-GQDs

The N-GQDs quantum dots were synthesized by employing a hydrothermal process. First, dopamine hydrochloride (0.125 g) and citric acid (0.5 g) were dissolved in 10 ml of ethanol, and the solution was then transferred into a 50 ml Teflon-lined stainless-steel autoclave. The autoclave was placed in an oven at 180 °C for 6 h and was then allowed to cool to room temperature naturally. The solution was thereafter centrifuged three times at 10,000 rpm for 10 mins. The supernatant was then removed and filtered using a syringe filtration membrane filter (0.22 μm).

2.4. Synthesis of $MoSe_2$

To prepare the $MoSe_2$ flakes, $MoSe_2$ powder was ground with 10 wt% of acetylene black (hereafter, AC) in ethanol by ball milling (8000D

Mixer/Mill®, SPEX® Sample Prep, America) for 12 h. Then, the powders of the $MoSe_2$ flakes were collected by centrifugation at 13,000 rpm (ethanol) for 10 mins and dried at 70 °C in a vacuum oven overnight, and these are named $MoSe_2$.

2.5. Synthesis of composite catalysts (LSC-N-GQDs-$MoSe_2$ and LSC-$MoSe_2$-N-GQDs)

First, synthesized LSC were high-energy milled with 10 wt% of AC in ethanol by ball milling using stainless steel balls for 12 h. Second, to find the optimum ratio of LSC/AC-N-GQDs (hereafter, LSC-N-GQDs), 0 wt%, 10 wt%, 20 wt% and 30 wt% and 40 wt% N-GQDs were mixed with LSC/AC (hereafter, LSC) using sonication. Third, different weight ratio of LSC and $MoSe_2$ (2:1, 1.5:1.5, and 1:2) were mixed by milling for 0.5 h to find the optimum weight ratio of LSC-$MoSe_2$. Next, the LSC with 10 wt%, 20 wt% and 30 wt% N-GQDs were milled with $MoSe_2$ according to the optimum weight ratio in ethanol using stainless steel balls for 0.5 h. Finally, the powders were collected by centrifugation at 13,000 rpm for 10 mins and were dried at 70 °C in a vacuum oven overnight for further analysis. The resulting composite was named LSC-N-GQDs-$MoSe_2$.

As a control sample, LSC/$MoSe_2$ and N-GQDs were mixed to synthesize LSC-$MoSe_2$-N-GQDs. First, synthesized pure LSC were high-energy milled with 10 wt% of AC in ethanol by ball milling using stainless steel balls for 12 h. Next, LSC was ground with $MoSe_2$ according to the optimum weight ratio (2:1) in ethanol for 0.5 h. The composite of LSC and $MoSe_2$ was named as LSC-$MoSe_2$. Thirdly, 20 wt% N-GQDs was mixed with the LSC-$MoSe_2$ by sonication for 90 mins. Finally, the powders were collected by centrifugation at 13,000 rpm for 10 mins and were dried at 70 °C in a vacuum oven overnight for further analysis.

2.6. Fabrication electrodes for electrochemical reaction

The generated LSC, $MoSe_2$, LSC-$MoSe_2$, LSC-N-GQDs-$MoSe_2$ catalysts were prepared as an ink by dispersing 10 mg of the catalyst in 1 ml of ethanol using bath sonication. Then, the catalyst ink was dropped on glassy carbon electrode (hereafter, GC electrode) with a loading mass of 0.1 mg. After the catalyst film dried in air, Nafion (5 wt%, 10 μl) was covered on the catalyst as a film. After the Nafion film dries, the obtained electrode was used as a work electrode in the electrochemical measurements. The electrodes for the overall water splitting were fabricated by dropping a catalyst ink on an Ni foam (1 * 1.5 cm^2). Ni foam as a substrate of the catalyst was pretreated by HCl in a water bath ultrasound for 5 mins, was washed by acetone three times, and dried in an ambient atmosphere. Then, the anode and cathode electrodes were prepared by coating a loading density of 1 $mg{\cdot}cm^{-2}$ ink on cleaned Ni foam, dried at 70 °C in a vacuum oven overnight, and coated with Nafion.

2.7. Material characterizations

The crystal structures for all powder samples were studied using an X-ray diffractometer system (Rigaku MAX 2500 V) using Ni Kα radiation at a scan rate of 1° min^{-1}. The morphologies of the catalysts were conducted using high-resolution transmission electron microscopy (JEOL JEM-2100 F) with selected area electron diffraction (SAED) and a Field Emission Scanning Electron Microscope (JEOL JSM-6700 F). The Raman spectra were obtained by a dispersive Raman microscope (SENTERRA Raman) with a 532 nm laser as an excitation source. The bonding state of the elements in the composites was observed via X-ray photoelectron spectroscopy (ThermoFisher K-alpha).

2.8. Electrochemical measurements

The electrochemical performance of the catalysts was investigated using the Ivium-n-Stat system in a typical three-electrode configuration that includes a Pt wire and an Ag/AgCl electrode (saturated KCl solution) as counter and reference electrodes, respectively. The work electrode is a GC electrode with a catalyst in a diameter of 2 mm. The GC electrode was coated by a catalyst with a loading mass of 0.1 mg. Then, linear sweep voltammetry (hereafter, LSV) measurements were conducted in 1.0 M KOH aqueous solution with a potential ranging from 0 to 0.8 V versus Ag/AgCl for OER and −0.8 V to −1.8 V versus Ag/AgCl for HER at a scan rate of 50 $mV{\cdot}s^{-1}$ with a rotation speed of 700 rpm. The electrochemical impedance spectroscopy (hereafter, EIS) was conducted at a 10 mV amplitude with a frequency ranging from 1 to 10 kHz. The double-layer capacitance (hereafter, C_{dl}) was calculated from circulation voltammetry (hereafter, CV) at a scan rate of 10, 20, 50, 100 and 200 $mV{\cdot}s^{-1}$. In the stability performance test, Ni foam with catalyst a loading density of 1 $mg{\cdot}cm^{-2}$ as anode and cathode electrodes were set in the two-electrode system. Chronopotentiometry (hereafter, CP) tests proceeded at a current density of 10 $mA{\cdot}cm^{-2}$ and 500 $mA{\cdot}cm^{-2}$ for 24 h at a rotation speed of 700 rpm using the Ivium-n-Stat system with a two-electrode setup in 1.0 M KOH solution.

3. Results and discussion

The bi-functional electrocatalyst is rationally designed by engineering a heterostructure comprised of $La_{0.5}Sr_{0.5}CoO_{3-\delta}$ (LSC) NPs and molybdenum diselenide ($MoSe_2$) with a small amount of N-doped graphene quantum dots (N-GQDs) to improve the charge transfer characteristics of the interface. Ball-milling was used to ensure better mechanochemical coupling and create intimate heterointerfaces with enhanced active sites for both reactions. Fig. 1 shows the schematic to synthesize the composites using a wet chemical method plate followed by ball milling. (Detailed experimental procedures are provided in the Experimental section.) Initially, N-GQDs were prepared using a mixture of citric acid and dopamine under hydrothermal conditions (Fig. 1a-i). High-resolution electron microscope (HR-TEM) images of the as-prepared N-GQDs show uniform particles with an average size of ~2 nm and good crystallinity with 0.21 nm lattice fringes corresponding to the (100) plane. High-resolution electron microscope (HR-TEM) images of the as-prepared N-GQDs show uniform particles with an average size of 2–3 nm and good crystallinity with 0.21 nm lattice fringes corresponding to the (100) plane. The size-distribution histogram of N-GQDs were obtained by counting 100 particles, shown in Fig. S1. Simultaneously, LSC NPs were prepared via a sol-gel method, followed by high-energy ball milling for 12 h to reduce the size of the particles (Fig. 1a-ii). Field emission scanning electron microscopy (FE-SEM) of the as-prepared LSC showed quite uniform particles with average measures of around 40 nm (Fig. 1b-i). The ball-milled LSC NPs were then mixed with different ratios of N-GQDs via sonication (Fig. 1a-iii). The $MoSe_2$ flakes were also prepared via ball milling (Fig. 1a-iv), which produced uniform and ultrafine 2D sheets of about 30 nm in average thickness and about 80 nm in average diameter (Fig. 1b-ii). Finally, different weight ratios of $MoSe_2$ are added to the LSC-N-GQDs in ethanol, followed by ball milling for 0.5 h to obtain LSC-N-GQDs-$MoSe_2$ composites (Fig. 1a-v). The LSC-N-GQDs-$MoSe_2$ composites were then centrifuged at 13,000 rpm for 10 mins, dried at 70 °C in a vacuum oven overnight to get the powder form. As evident in Fig. 1c, the LSC-N-GQDs NPs were attached to the surface of $MoSe_2$ nanosheets to form a heterostructured interface.

The powder X-ray diffraction (XRD) patterns of the as-synthesized $MoSe_2$, LSC, and LSC-N-GQDs-$MoSe_2$ composites were collected to investigate the crystal structure, as illustrated in Fig. S2. The pristine LSC NPs show the most intense diffraction peak at 33°, 47°, and 59° (JCPDS Card No. 36-1392), corresponding to the (104), (024), and (214) planes, respectively, of the monoclinic structure. All of the peaks from the pristine $MoSe_2$ could be indexed to the 2 H-$MoSe_2$ phase (JCPDS Card No. 87-2419). No characteristic peaks for impurities are observed, demonstrating that the as-synthesized samples are composed of only LSC and $MoSe_2$. The LSC-N-GQDs-$MoSe_2$ composites showed several peaks corresponding to LSC and $MoSe_2$ without any additional peaks, demonstrating that additional phases were not formed during ball

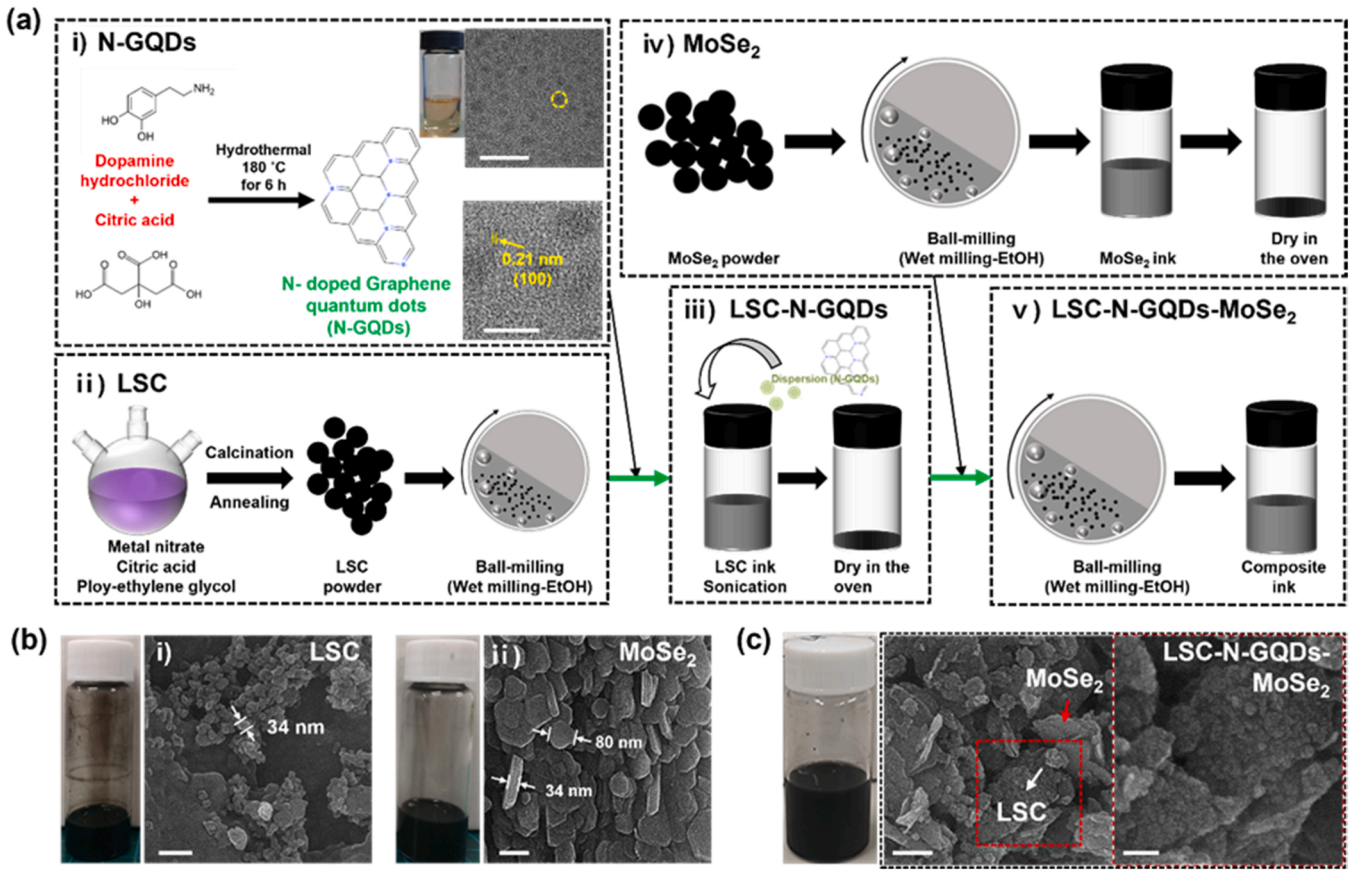

Fig. 1. (a) Schematic of the synthesis of LSC-N-GQDs-$MoSe_2$ NPs. (b) SEM images of LSC NPs and $MoSe_2$ NPs. (c) SEM images of LSC-N-GQDs-$MoSe_2$ NPs. (scale bar: (a) 20 nm top and 5 nm bottom side TEM images, (b) 100 nm left and 100 nm right side SEM images, (c) 100 nm left and 50 nm right side SEM images).

milling.

A more detailed morphology of the LSC-N-GQDs-$MoSe_2$ composites was obtained via HR-TEM images with an elemental analysis conducted via energy-dispersive X-ray spectroscopy (EDX), as shown in Fig. 2. The resulting composites were seen to have a roughly Janus-like structure, wherein LSC nanoparticles were decorated by the $MoSe_2$, which is consistent with the structure seen in the SEM images (Fig. 1c). The high magnification image shows that both materials exhibit good crystallinity, as indicated by lattice-plane spacings of 0.27 and 0.29 nm, which correspond to the LSC (110) and $MoSe_2$ (100) planes, respectively. The fast Fourier transform (FFT) patterns (Fig. 2b) also confirm that the nanocrystals exhibit good crystallinity and a composite nature. At the interface of the LSC and $MoSe_2$, a very thin layer of N-GQDs with a thickness of 2–3 nm were observed. Actually, it is quite difficult to prove the presence of N-GQDs at the interface, but the high-magnification TEM image clearly shows the existence of hexagonal rings with lattice defects, confirming the existence of the N-GQDs at the interface of the LSC and $MoSe_2$. To support the presence of N-GQDs at the interface, the LSC-N-GQDs sample was prepared and TEM measurement were carried out, as shown in Fig. S3. High-magnified HR-TEM image of LSC-N-GQDs confirms a distinct lattice fringe of LSC (0.27 nm and 0.45 nm) and N-GQDs (0.21 nm) without an amorphous layer of LSC, showing the crystalline interface between LSC and N-GQDs (Fig. 3b and c). This shows that the surface of LSC NPs was well covered with N-GQDs. The X-ray spectroscopy (STEM-EDS) mapping (Fig. 2c) of the LSC-N-GQDs-$MoSe_2$ composites confirms that nitrogen and carbon atoms were exactly in the same position, indicating that the N had been doped into the N-GQDs. The presence of the N-GQDs at the interface was also investigated via Raman spectra, as plotted in Fig. 2d. The pristine N-GQDs samples exhibited D and G bands at 1370 and 1583 cm^{-1}, respectively. The intensity of the D band is strongly associated with the disorder degree of graphene, while the G band corresponds to the stretching vibration mode $E_{2\,g}$ for sp^2 carbon domains. Compared to pristine N-GQDs, the D and G bands of the LSC-N-GQDs-$MoSe_2$ composites shows a lower frequency peak shift (16 cm^{-1}) with a lower (I_D/I_G) ratio, indicating the formation of more graphene domains and an improvement in the conductivity of the N-GQDs [48,49]. Also, the downshift of the D and G bands indicates the N-GQDs have intimate contact hybridization with an electron acceptor-donor component, which is reliable evidence of the charge transfer from LSC to $MoSe_2$ [50–52]. The more details of Raman spectra of LSCO, $MoSe_2$ and LSC-N-GQDs-$MoSe_2$ NPs are shown in Fig. S4.

The microstructures of the $MoSe_2$ near the interface of the N-GQDs and $MoSe_2$ were also investigated in detail, as shown in Fig. 2e. As seen in the TEM results, the $MoSe_2$ in the area away from the interface was seen to have a 2 H-phase, while near the interface, the phase changed to the 1 T phase, i.e. the trigonal lattice area of the 1 T phase with corresponding lattice planes. The distance of the Mo-Mo atom and Se-Se atom was about 0.55 and 0.33 nm, respectively, which corresponds to the $\sqrt{3}a \times a$ form in the 1 T-$MoSe_2$ structure [53,54]. However, in LSC-$MoSe_2$, the interface of the $MoSe_2$ displayed a common honeycomb lattice area of the trigonal prismatic coordination in the 2 H phase, as shown in Fig. S5. This phase change is probably due to a strong electronic coupling effect and an interfacial charge transfer from the N-GQDs that affects the electronic state of the $MoSe_2$ causing a chain clusterization of the metal atoms and the formation of a superlattice in the $MoSe_2$ owing to the Jahn-Teller instability [55,56].

The prepared LSC, LSC-$MoSe_2$, and LSC-N-GQDs-$MoSe_2$ heterostructures were then coated onto a glassy carbon electrode (GCE), and the hydrogen evolution reaction (HER) and oxygen evolution reaction (OER) were evaluated under alkaline conditions (pH = 13.2) in a three-electrode configuration. Initially, the OER performances were

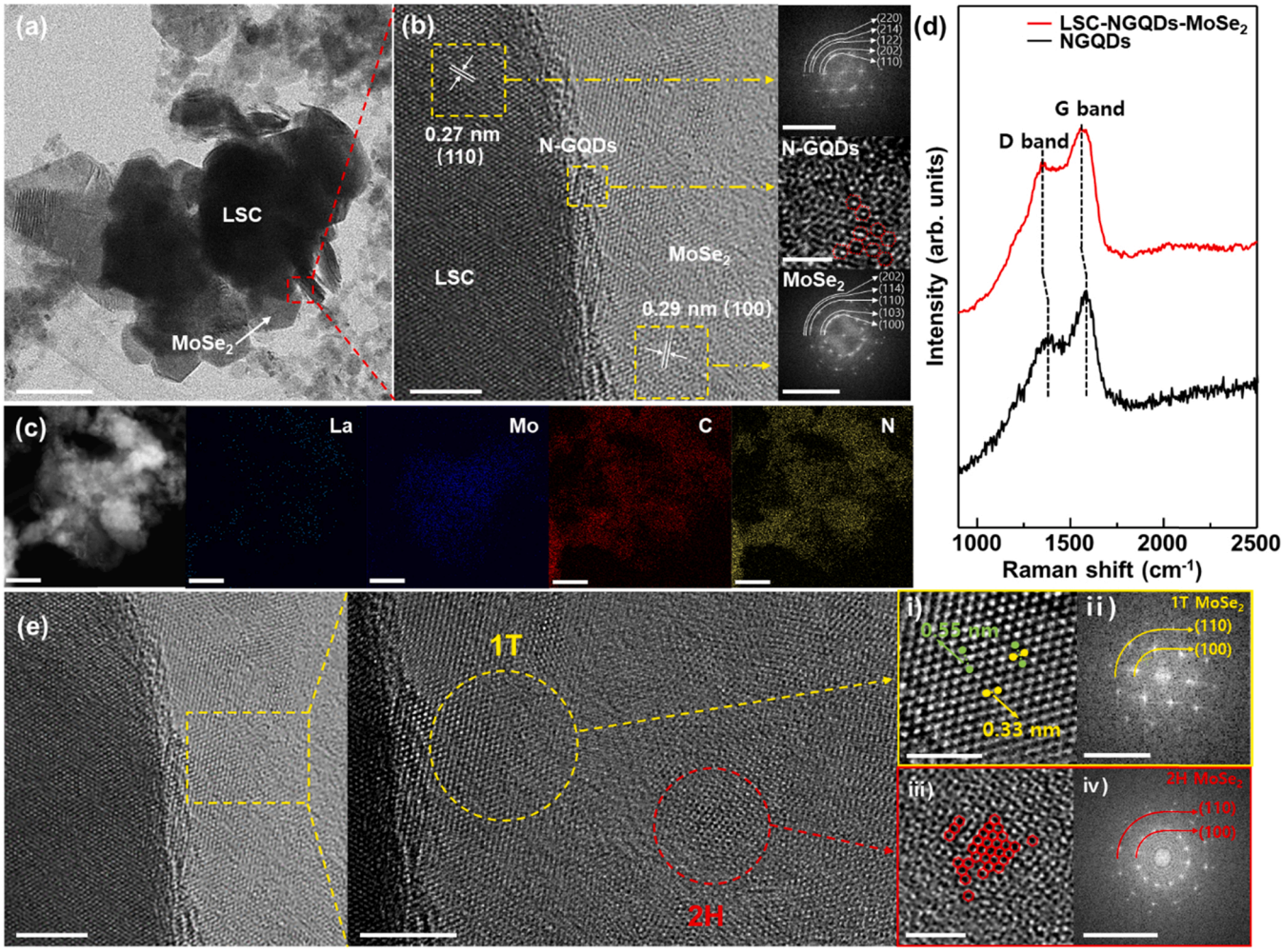

Fig. 2. (a) TEM and (b) HR-TEM images of LSC-N-GQDs-$MoSe_2$ NPs with FFT pattern of LSC (right-top), TEM image of N-GQDs (right-middle) and FFT pattern of $MoSe_2$ (right-down). (c) STEM-EDS mapping images and elemental distribution of LSC-N-GQDs-$MoSe_2$ NPs: region of mapping and La, Mo, C, and N. (d) Raman spectra of pure N-GQDs and LSC-N-GQDs-$MoSe_2$ NPs. (e) HR-TEM images of 1 T and 2 H phase of $MoSe_2$ in composite. (scale bar: (a) 200 nm, (b) 5 nm left and 2 nm right side TEM images, 10 nm^{-1} top and 10 nm^{-1} bottom side FFT patterns, (c) 100 nm mapping images, (e) 5 nm left and 5 nm middle side TEM images, (e-i) 2 nm, (e-ii) 10 nm^{-1}, (e-iii) 2 nm and (e-iv) 10 nm^{-1}).

investigated by obtaining linear sweep curves (LSV) at a 50 $mV{\cdot}s^{-1}$ scan rate on the reversible hydrogen electrode (RHE) scale in a 1.0 M KOH solution, as plotted in Fig. 3a. The corresponding Tafel plots were derived from the LSV curves in Fig. 3b. As reference, a commercial IrO_2/C sample exhibited good OER performance with an overpotential of 240 mV vs. RHE and a Tafel slope of 54 $mV{\cdot}dec^{-1}$, which is comparable to that of commercial catalysts [19,20]. However, the overpotential and the Tafel slope of the pristine LSC increased to 336 mV and 84 $mV{\cdot}dec^{-1}$, respectively. When the composites were synthesized using LSC and $MoSe_2$ by ball milling (the optimum weight percent weight ratio of the LSC and $MoSe_2$ shown in Fig. S6), they decreased to 307 mV and 59 $mV{\cdot}dec^{-1}$, respectively. The enhancement of the electrochemical performance may be ascribed to the formation of mechanically stamped heterostructures during ball milling. At the interface of the two materials, the charge transfer occurs due to the difference of the work functions, yielding changes in the t_{2g} and e_g orbital occupancy, thereby, improving the OER performance [41].

Finally, the OER process catalyzed by the LSC-N-GQDs-$MoSe_2$ was evaluated under the same conditions. To find the optimum weight percent of the N-GQDs, the N-GQDs were decorated onto the LSC nanoparticles, and the OER performances were tested according to the concentration of N-GQDs, as plotted in Fig. S7a. At 20 wt%, the overpotential decreased to 323 mV. However, a further increase to 40 wt% of the N-GQDs significantly increased the overpotential to 349 mV. The optimum weight percent of the N-GQDs was also evaluated at LSC-N-GQDs-$MoSe_2$, plotted in Fig. S8a. As the weight percentage of N-GQDs was increased to 20 wt%, the overpotential at a current density of 10 $mA{\cdot}cm^{-2}$ was decreased measured to be about 302 mV, which is the lowest value excluding that of commercial IrO_2-based catalysts. Nevertheless, it is comparable to that found in recent reports for OER catalysts based on non-precious metal-oxides, chalcogenides, nitrides, and phosphides under similar alkaline media (Table S1). The LSC-N-GQDs-$MoSe_2$ composites also show a Tafel slope of 51 $mV{\cdot}dec^{-1}$, which is smaller than that of IrO_2 (54 $mV{\cdot}dec^{-1}$). This indicates faster electrocatalytic reaction kinetics [57], which reduces the voltage at a high current density. However, at 30 wt% N-GQDs, the performance was degraded. This may be due to high N-GQDs coverage which cover active sites of LSC and $MoSe_2$ [58].

Fig. 3c shows the HER performance of the LSC, $MoSe_2$, LSC-$MoSe_2$, and LSC-N-GQDs-$MoSe_2$ heterostructured catalysts obtained at the same 1.0 M KOH conditions. The Tafel plots were derived from the LSV profiles, as shown in Fig. 3d. To evaluate the electrocatalytic activity toward HER, a Pt wire was used as a counter electrode and the current density versus potential was measured at a scan rate of 50 $mV{\cdot}s^{-1}$ at room temperature. For the pristine LSC, a current density of -10 $mA{\cdot}cm^{-2}$ was achieved at an overpotential (η) of 438 mV vs RHE, and a Tafel slope

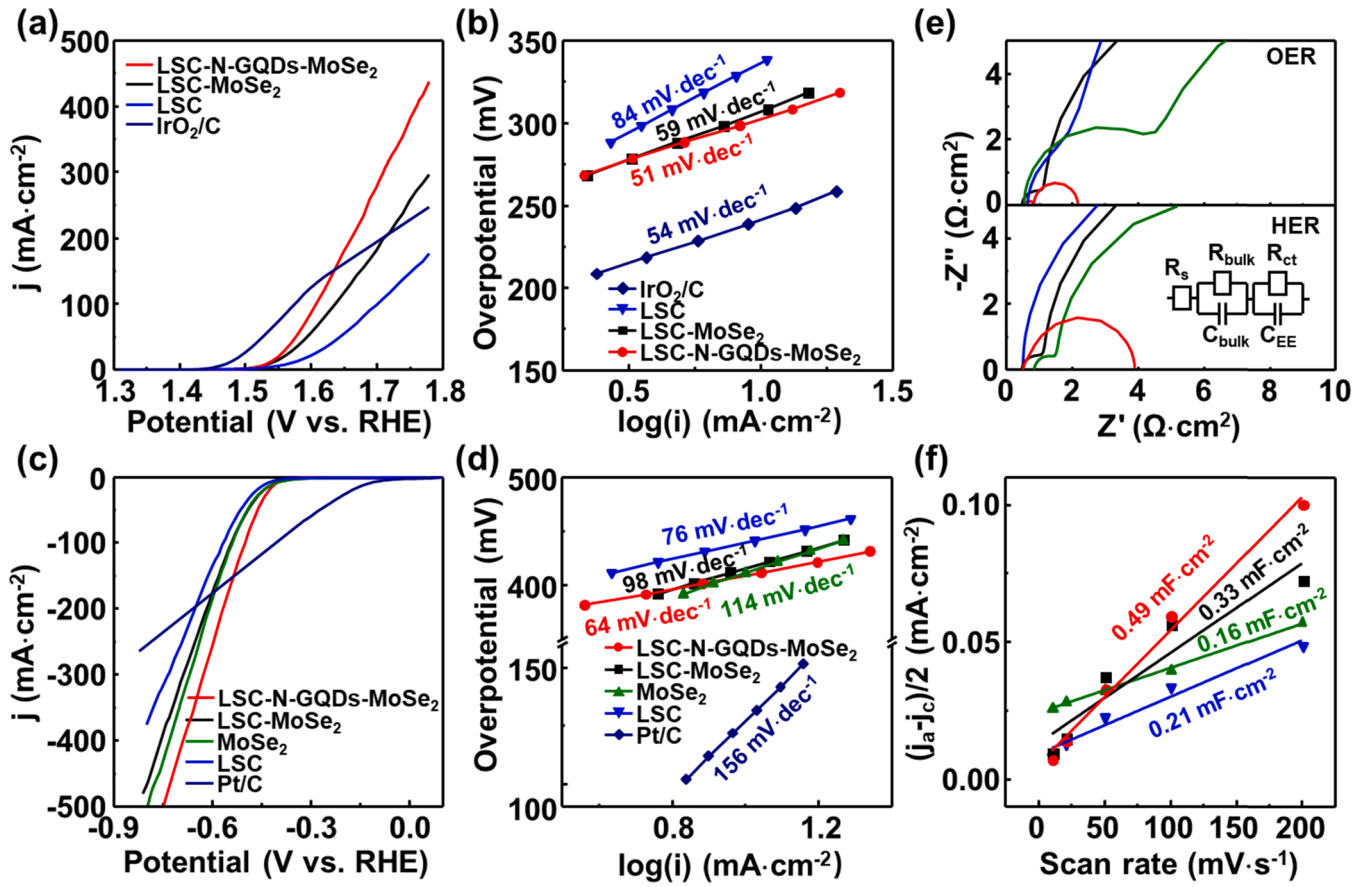

Fig. 3. Electrochemical performances of various catalysts. (a) OER polarization curves of various catalysts in 1.0 M KOH. (b) Tafel analysis of the OER profiles. (c) HER polarization curves of various catalysts in 1.0 M KOH. (d) Tafel analysis of the HER profiles. (e) Nyquist plots of LSC, $MoSe_2$, LSC-$MoSe_2$ and LSC-N-GQDs-$MoSe_2$. (f) electrochemical double-layer capacity (C_{dl}) of LSC, $MoSe_2$, LSC-$MoSe_2$ and LSC-N-GQDs-$MoSe_2$. (j_a: anodic current density; j_c: cathodic current density).

of 76 mV·dec^{-1} was measured. For the pristine $MoSe_2$, an overpotential of 412 mV was measured, and it was lower than that of the pristine LSC. This may be ascribed to the Gibbs free energy for atomic hydrogen adsorption which is closer to zero and a high hydrogen coverage on the $MoSe_2$ active sites [59]. However, the Tafel slope was measured to be 114 mV·dec^{-1}, meaning that a higher voltage at a high current density was required, compared to pristine LSC. When the composites were produced, it showed a quite low overpotential and Tafel slope of 415 mV and 98 mV·dec^{-1}, respectively. This may be ascribed to the electron transfer from the LSC, which results in a higher conductivity of the $MoSe_2$ [41]. Regarding the electrochemical performances according to the N-GQDs concentration shown in Fig. S8b, the LSC-N-GQDs-$MoSe_2$ composites with 20 wt% N-GQDs exhibited an overpotential of 409 mV. The observed HER performance is also comparable to that of recent report on HER catalysts based on non-precious metal-oxides, chalcogenides, nitrides, and phosphides in similar alkaline media (Table S1). The Tafel slope was also measured to be about 64 mV·dec^{-1}, which is much lower than that of the others. Although the commercial Pt/C exhibited the lowest overpotential, a lower Tafel slope of the composites indicates a low voltage is required at a high current density. As a control sample, LSC-$MoSe_2$-N-GQDs with 20 wt% N-GQDs were synthesized, as shown in Fig. S9a, the electrochemical performance was evaluated, plotted in Figs. S9b and S9c. When N-GQDs were decorated onto the LSC-$MoSe_2$, the overpotentials for HER and OER were significantly decreased, indicating that the performance was optimized when N-GQDs were existed in the interlayer.

To further explore the kinetic properties of the prepared catalysts, electrochemical impedance spectroscopy (EIS) curves for OER and HER were obtained under potentials of 0.55 V and − 1.38 V vs. Ag/AgCl, respectively, to evaluate the charge transfer resistance (R_{ct}). Figs. 3e and S10 show the Nyquist plots of LSC, $MoSe_2$, LSC-$MoSe_2$, and LSC-N-GQDs-$MoSe_2$, which exhibited R_{ct} between the catalysts on the GC electrode and the electrolyte of 1.0 M KOH. The equivalent circuit fitting results of OER and HER for Nyquist plots were shown in Supplementary Table S2 and Table S3, respectively. From the Nyquist plots for both OER and HER, LSC-N-GQDs-$MoSe_2$ exhibited the smallest R_{ct} compared to LSC, $MoSe_2$, and LSC-$MoSe_2$. This implies that the electron transport in the composites is enhanced by the formation of the N-GQDs at the interface of the LSC and $MoSe_2$. Moreover, cyclic voltammetry (CV) curves (Fig. S11) at different scan rates were measured to obtain the electrochemical double-layer capacitance (C_{dl}) to evaluate the electrochemical active surface areas (ECSAs) [60]. The current densities are normalized by the ECSA or mass of the catalyst to determine the specific activity or mass activity at a potential of 0 V versus Ag/AgCl. As shown in Fig. 3f, the C_{dl} of 0.49 mF·cm^{-2} for the LSC-N-GQDs-$MoSe_2$ is more than 1.4 times that of the others, confirming that the LSC-N-GQDs-$MoSe_2$ composites have more active sites.

X-ray photoemission spectroscopy (XPS) was employed to investigate the chemical and electronic states to elucidate the interface interactions and charge transfer mechanism at the interface. Fig. 4 displays the La 3*d*, Co 2*p*, Se 3*d*, Mo 3*d*, and O 1*s* core-level spectra of the LSC, $MoSe_2$, LSC-$MoSe_2$, and LSC-N-GQDs-$MoSe_2$ catalyst composites. As shown in Fig. 4a, the peaks located at 834.2 eV and 851.1 eV of the pristine LSC correspond to two doublets of $3d_{5/2}$ and $3d_{3/2}$ of La^{3+} oxidation state with strong shake-up satellite peaks (837.8 and 854.7 eV), respectively. After the formation of the composites, the La 3*d* peaks shifted 0.7 eV and 1.3 eV toward a higher binding energy in the LSC-$MoSe_2$ and LSC-N-GQDs-$MoSe_2$ composite, respectively. The shift of

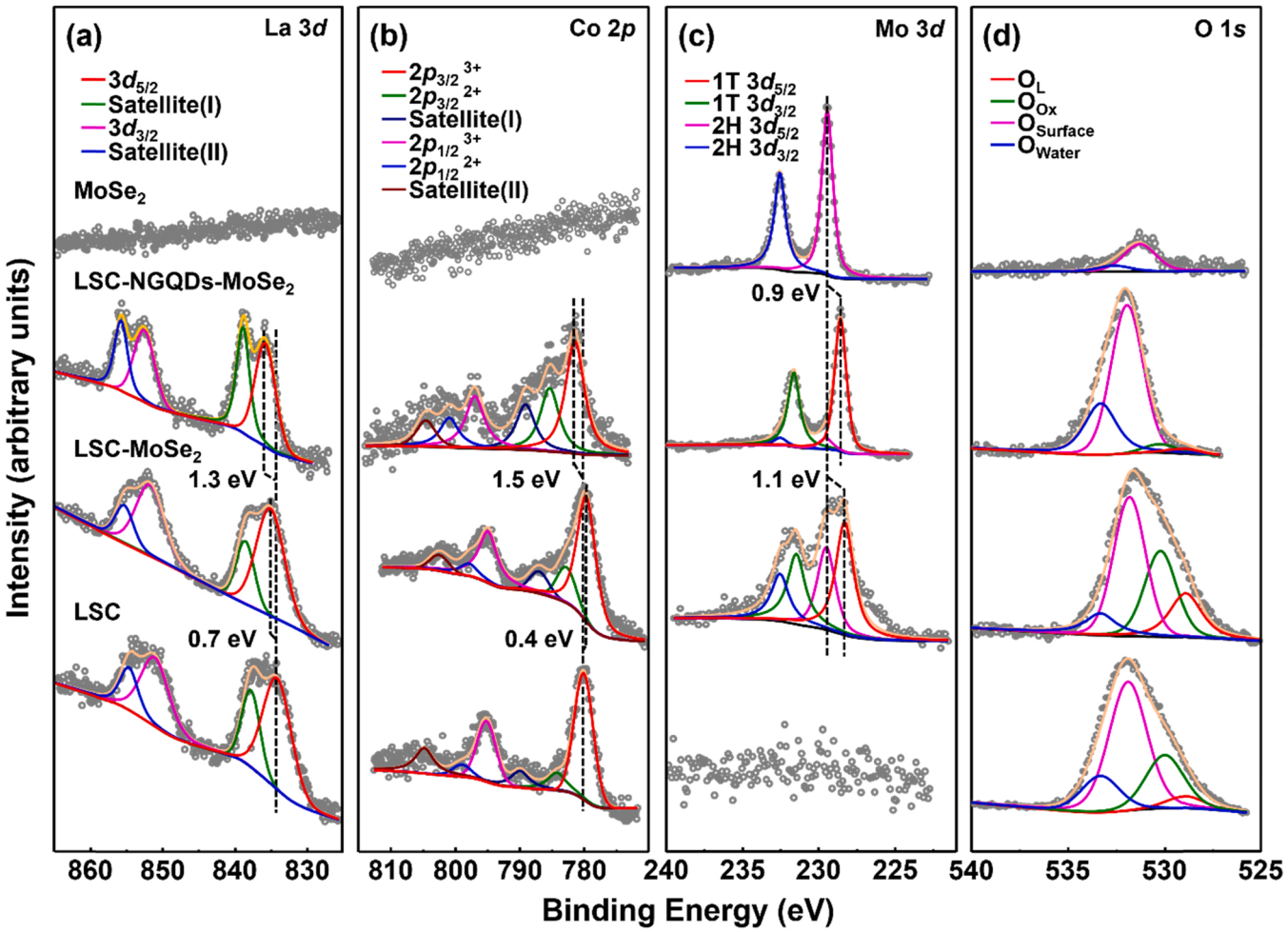

Fig. 4. Comparison of the XPS spectra of LSC-$MoSe_2$, LSC-N-GQDs-$MoSe_2$, LSC and $MoSe_2$. (a) La 3*d*, (b) Co 2*p*, (c) Mo 3*d*, and (d) O 1*s* core levels.

the La 3*d* peaks implies that the electrons leave the surface [61]. Fig. 4b shows that the deconvoluted Co 2*p* consist of two spin-orbit doublets, Co $2p_{3/2}$ and Co $2p_{1/2}$ (Co^{3+} and Co^{2+}) with two satellites peaks. In pristine LSC, the Co^{3+} and Co^{2+} of the LSC are positioned at 780.06/795.2 eV and 784.24/799 eV, respectively. For the LSC-$MoSe_2$ composites, the Co^{3+} and Co^{2+} were located at 779.62/794.93 eV and 782.75/797.89 eV, respectively, indicating the downshift of Co^{3+} (~ 0.4 eV) and Co^{2+} (~1 eV) binding energy in the LSC-$MoSe_2$ relative to pristine LSC. This shift in the XPS peak was attributed to the change in the oxidation state of the LSC owing to the presence of $MoSe_2$. Interestingly in LSC-N-GQDs-$MoSe_2$, the Co^{3+} and Co^{2+} were located at 781.45/797.01 eV and 785.37/801 eV, respectively, indicating a Co^{3+} (~ 1.5 eV) and Co^{2+} (~ 2 eV) binding energy upshift in LSC-N-GQDs-$MoSe_2$ relative to pristine LSC and LSC-$MoSe_2$, which is in agreement with the shift of the La 3*d* peaks. By comparing the Co 2*p* spectra volume fraction, the $Co^{3+}/(Co^{2+} + Co^{3+})$ ratios of the LSC, LSC-$MoSe_2$ and LSC-N-GQDs-$MoSe_2$ were found to be 0.62, 0.54 and 0.67, respectively, indicating dominant higher oxidation Co^{3+} cations species in LSC-N-GQDs-$MoSe_2$ composites. Thus, the Co 2*p* spectra of the LSC-N-GQDs-$MoSe_2$ have higher oxidation states due to the stronger electronic coupling between the LSC and N-GQDs interface compared to that for the LSC and LSC-$MoSe_2$, owing to the electron transfer at the interface of the LSC to the N-GQDs. Also, there is a gradual increase in co-existences of Co^{2+} and Co^{3+} from LSC to LSC-$MoSe_2$, and then to LSC-N-GQDs-$MoSe_2$ (Fig. 4b). Thus, the N-GQDs incorporated between the LSC and $MoSe_2$ enhanced the charge imbalance to enhance the cation redox reaction, oxidation ability, and electronic properties, which is beneficial to achieve better electrocatalytic performance [62]. Also, due to the stronger electronegativity of the N-GQDs in the LSC-N-GQDs-$MoSe_2$ composites, the decreased electron density on the Co sites makes the Co ions more electrophilic in nature to induce water molecule adsorption by modulating the electronic structure of the Co by upshifting the d-band center [63–65]. Similarly, the modulation of the electronic structure of the Co were also reported in previous papers, where electron-withdrawing groups such as Mo, Ce, Cu promoted OER reaction on Co surface by coupling Co to the groups [66–70].

As shown in Fig. 4c, the Mo 3*d* spectra of pristine $MoSe_2$ shows two characteristic peaks at binding energies of 229.4 and 232.6 eV, assigned to the Mo $3d_{5/2}$ and Mo $3d_{3/2}$ orbitals, respectively, indicating a + 4-valence state of the Mo as well as the presence of the 2 H $MoSe_2$ phase [59]. Compared to pristine $MoSe_2$, the Mo $3d_{5/2}$ and Mo $3d_{3/2}$ peaks of the LSC-$MoSe_2$ composites were broadened and deconvoluted into four peaks. That is, peaks at 228.31 and 231.48 eV correspond to 1 T phase $MoSe_2$, and peaks at 229.51, and 232.55 eV correspond to 2 H phase $MoSe_2$, respectively [71]. The induced evolution of the 1 T-$MoSe_2$ was due to the in-situ phase transition in the $MoSe_2$ by electron transfer from the LSC to Mo and a heterostructure formation, as per previous studies [41,72]. Interestingly in the LSC-N-GQDs-$MoSe_2$ composites, the Mo $3d_{5/2}$ and Mo $3d_{3/2}$ peaks were shifted by ~ 0.9 eV to 228.59 and 231.64 eV respectively and correspond to 1 T phase $MoSe_2$. The electron transfer between the N-GQDs and Mo can be a dominant factor in improving the intrinsic electrocatalytic nature and activity of the LSC-N-GQDs-$MoSe_2$ composites, which induces semiconducting (2 H) to a metallic (1 T) phase transition in $MoSe_2$ [56,73]. In addition, the characteristic peaks arising from Se $3d_{5/2}$ and Se $3d_{3/2}$ orbitals are located at 55.02 and 55.88 eV and reveal the −2 oxidation state of Se,

corresponding to the Se $3d_{3/2}$ and Se $3d_{5/2}$ spectra, respectively (Fig. S12). Similarly, in the Se 3*d* spectrum of the LSC-$MoSe_2$ composites, two peaks at 53.99 and 54.85 eV correspond to the 1 T phase of $MoSe_2$, and the other two peaks at 55.02 and 55.84 eV are assign to the 2 H phase $MoSe_2$. While the Se $3d_{3/2}$ and Se $3d_{5/2}$ peaks of LSC-N-GQDs-$MoSe_2$ composites were ~ 0.8 eV downshifted to 54.18 and 55.05 eV, confirming the presence of 1 T phase $MoSe_2$ via a chemical coupling effect between the formed heterostructure. The coexistence of the 1 T and 2 H phase of the $MoSe_2$ in LSC-$MoSe_2$ (Fig. S5) and LSC-N-GQDs-$MoSe_2$ (Fig. 2e) composites was also verified via HR-TEM image.

Finally, the O 1*s* core-level spectra were analyzed to investigate the surface oxygen species of the catalysts, which is a crucial parameter to control the electrochemical performance. In pristine LSC, the high-resolution O 1*s* XPS spectrum exhibits four pronounced peaks located at 529.9, 531.3, 532.6, and 533.5 eV representing lattice oxygen (O_L), highly oxidative oxygen (O_{Ox}), surface-active oxygen ($O_{Surface}$), and adsorbed water (O_{water}), respectively (Fig. 4d). The ratio of the surface-active oxygens to the lattice oxygens can be used as an indicator for evaluating the performance. After introducing only $MoSe_2$, the surface active oxygens decreased, however, incorporating N-GQDs between the LSC and $MoSe_2$ (LSC-N-GQDs-$MoSe_2$) increased the surface active oxygens, indicating higher hydroxide species adsorption to improve the intrinsic electrochemical performance [41].

In addition, XPS spectra of N 1*s* and C 1*s* of N-GQDs and LSC-N-GQDs-$MoSe_2$ composite were measured, as shown in Fig. S13. In N 1*s*, the peaks located at 398.6, 399.6 and 400.8 eV at N-GQDs are attributed to pyridinic N, pyrrolic N, and graphitic N, respectively [74]. In LSC-N-GQDs-$MoSe_2$ composite, the peak of pyridinic N was shifted by 0.3 eV toward lower binding energy because the nitrogen atoms in the carbon network interacts metallic interface as charge acceptor-donor [75,76]. The peak intensity of pyridinic N and graphitic N was increased, implying that more graphene domains were produced in the composite by ball-milling process, which could provide more electrophilic active site to facilitate hydrogen absorption for HER [77]. The C 1*s* spectra consisted of five peaks at 285.5, 285.6, 286.5, 287.6, and 289 eV, corresponding to C–C, C–N, C–O, C═O, and O–C═O groups, respectively [74]. The C-N peak was shifted by 0.2 eV toward lower binding energy, consistent with pyridinic N in LSC-N-GQDs-$MoSe_2$ composite. The peak intensity of O–C═O was increased, but the C═O was decreased compared to pristine. This may be attributed to ball-milling process where hydroxyl group were introduced in the composite [78]. Overall, in composite, the N 1*s* and C 1*s* XPS peaks shifted toward lower binding energies, indicating that the electron transfers occurred onto the N-GDQs' surface, where N atoms present in GQDs improves the electron transfer rate via providing conductivity, and high mobility of charge carriers [79–82].

Overall, a substantial shift was observed in the core level spectra of La 3*d*, Co 2*p*, Mo 3*d*, Se 3*d*, and O 1*s* after the N-GQD bridge formation between the LSC and $MoSe_2$ (LSC-N-GQDs-$MoSe_2$). All these observations suggest that introducing the N-GQDs between LSC and $MoSe_2$ was helpful in modulating the electronic structure of the Co central metal in LSC and Mo sites in $MoSe_2$ as the main active site in the electrocatalysis process. In addition, the formation of a heterostructure was also helpful to regulate the electronic structure of the interface to improve the charge transfer characteristics from the LSC to $MoSe_2$. The positive shifts of Co 2*p* orbital and the negative shifts of Mo 3*d* orbital indicate the transfer of electrons from Co to Mo through the N-GQD interface, which leads to a positive charge of the Co center in the LSC catalyst, which is conducive to the adsorption of OH^-, and the negative charge of the Mo center, which is conducive to the adsorption of H^+. The enhanced charge transport is consistent with the energy band alignment at the interface of the LSC, N-GQDs, and $MoSe_2$, as shown in Fig. S14 [27,83–85].

Finally, the operational stability and durability of the composites were investigated by taking chronopotentiometry measurements in 1.0 M KOH solution under 10 $mA{\cdot}cm^{-2}$ and 500 $mA{\cdot}cm^{-2}$. It was measured in a two-electrode setup using LSC-N-GQDs-$MoSe_2$ catalysts coated onto Ni foam as both anodes and cathodes. At a current density of 10 $mA{\cdot}cm^{-2}$, the cell voltage of the LSC-N-GQDs-$MoSe_2$ was about 1.57 V, and there was no change in the voltage during 24 hr, as shown in Fig. 5b. At a high current density of 500 $mA{\cdot}cm^{-2}$, the voltage was increased to about 2.47 V. However, there was still no change in the voltage during 24 hr. The Supplementary video 1 also showed that a lot of hydrogen and oxygen bubbles were generated at both electrodes. This result revealed that the LSC-N-GQDs-$MoSe_2$ composite showed a high stability at a high current density. Interestingly, the SEM images after 24 h of continuous testing at a high current density of 500 $mA{\cdot}cm^{-2}$ showed that some catalysts were peeled off from the Ni-foam. This may imply an enhancement in the electrocatalytic performance during the stability test because the electrochemical performance was not degraded. Thus, with better adhesion properties, it is expected that the cell voltage can be further decreased.

Supplementary material related to this article can be found online at doi:10.1016/j.nanoen.2022.107117.

For further investigation of the stability, the XRD and XPS measurements after 24-hr stability test at high current density of 500 $mA{\cdot}cm^{-2}$ were carried out, shown in Figs. S15 and S16, respectively. In Fig. S15, the diffraction peaks at 33°, 47°, and 59° are indexed to the (104), (024), and (214) planes of LSC (JCPDS Card No. 36–1392), respectively. In addition, the peaks at 27.6°, 37.9° and 55.8° were corresponded to (004), (103), and (008) planes of $MoSe_2$ (JCPDS Card No. 87-2419), respectively. The peaks were not changed in the intensity and position, and no other phase was found after long-term stability test. In the XPS results, the spectra of Co 2*p* and Mo 3*d* exhibited negligible changes after 24-hr stability test. The ratio of $Co^{3+}/(Co^{2+} + Co^{3+})$ was about 0.65, similar with before the test. Thus, the higher oxidation states of Co species due to the electron transfer between LSC and N-GQDs are not changed after stability test. In addition, the 1 T phase of $MoSe_2$ still appear in the spectrum after long-term test. This result illustrated that our catalyst showed great stability at high current density.

4. Conclusion

In summary, we have reported on the facile synthesis of composites composed of LSC and $MoSe_2$ as efficient bifunctional catalysts that operate at a large current density of 500 $mA{\cdot}cm^{-2}$ by exploiting the electronic charge-transfer across the interface in terms of the interfacial band alignment. Atomically precise interfaces were formed by incorporating a very thin layer (2–3 nm) of N-GQDs between the LSC and $MoSe_2$, and the Raman spectra revealed the downshift of the D and G bands, indicating an increase in the conductivity of the N-GQDs due to the electron transfer from LSC to N-GQDs. HR-TEM measurements showed the presence of a 1 T $MoSe_2$ phase near the N-GQDs. The LSC-N-GQDs-$MoSe_2$ composites with 0.2 wt% N-GQDs were optimized as bifunctional catalysts for the lowest overpotentials (409 mV and 302 mV) at 10 $mA{\cdot}cm^{-2}$ for HER and OER, respectively. Although the values were not good when compared to commercial samples (Pt/C and IrO_2/C), the electrocatalyst showed smaller Tafel slopes of 64 $mV{\cdot}dec^{-1}$ and 51 $mV{\cdot}dec^{-1}$, respectively. Thereby, the overpotentials are much lower at a large current density of 500 $mA{\cdot}cm^{-2}$.

With XPS measurement, the charge transfer across the interface through the N-GQD layer was investigated. By incorporating N-GQDs, La 3*d* and Co 2*p* peaks shifted toward a higher binding energy, and the population of Co^{3+} cations increased, indicating the promotion of the electron transfer from LSC to N-GQDs, which is also evident via Raman spectroscopy. The transferred electrons are then transferred to $MoSe_2$, leading to a phase change of 2 H to 1 T $MoSe_2$ for simultaneous OH^- and H^+ adsorption, as shown in Mo 3*d* spectra. Combined with the conductive N-GQDs interface, the LSC-$MoSe_2$ heterostructure exhibited an outstanding catalytic activity, high stability, rapid charge transfer ability, and faster catalytic kinetics towards HER and OER in alkaline solution. This study offers a quite simple and efficient approach to boost

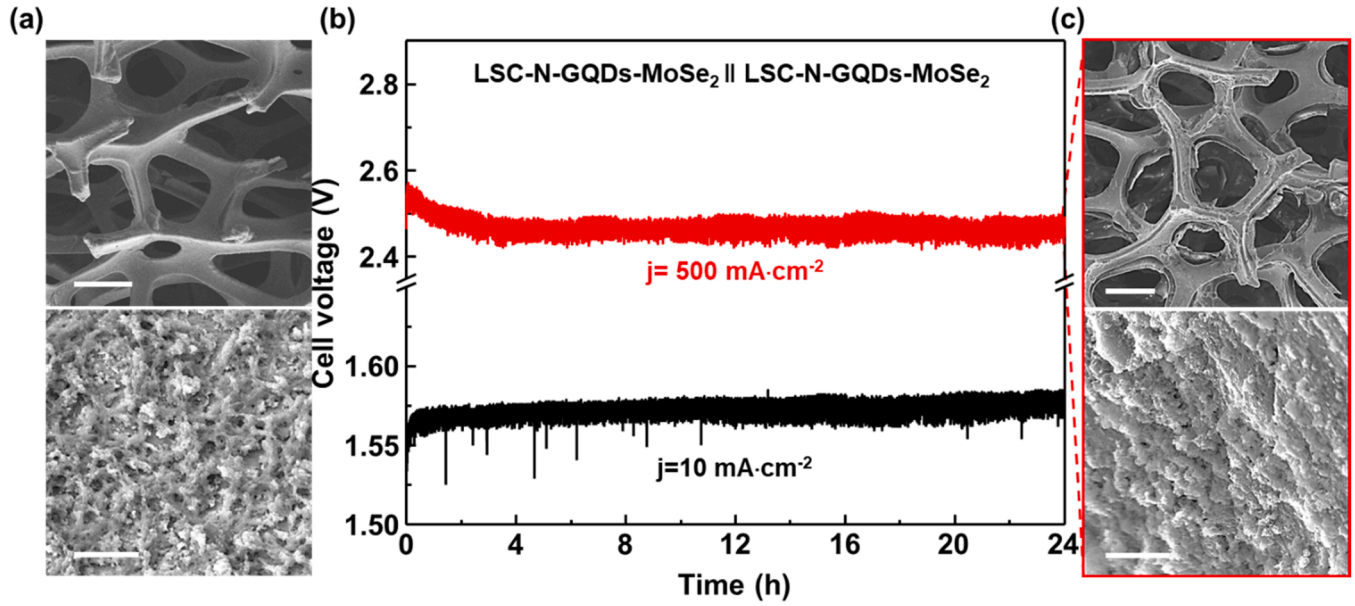

Fig. 5. (a) SEM images before the stability test. (b) Chronopotentiometric stability profiles measured at 500 mA·cm^{-2} for 24 h.(c) SEM images the stability test). (Scale bar: (a) 100 μm top and 5 μm bottom side SEM images, (c)200 μm top and 2 μm bottom side SEM images).

the interfacial charge transfer and catalytic activity in heterostructured bifunctional electrocatalysts.

CRediT authorship contribution statement

Chen Tian Cao: Formal analysis, Data curation, Investigation, Writing – original draft. **Sun-Woo Kim:** Formal analysis, Investigation, Writing – original draft. **Hee Jun Kim:** Data curation, Investigation. **Rahul Purbia:** Data curation. **Sang Heon Kim:** Data curation. **Dokyoung Kim**: Data analysis. **Kyoung Jin Choi:** Data analysis. **Hyesung Park:** Project administration, Funding acquisition, Writing – original draft. **Jeong Min Baik:** Conceptualization, Supervision, Project administration, Funding acquisition, Writing – original draft, Writing – review & editing.

Declaration of Competing Interest

The authors declare that they have no known competing financial interests or personal relationships that could have appeared to influence the work reported in this paper.

Acknowledgements

C.T.C and S.W.K contributed equally to this work. All authors discussed the results, wrote and commented on the manuscript.

This work was supported by the Mid-Career Researcher Program through a National Research Foundation of Korea (NRF) grant funded by the Korean government (NRF-2019R1A2C2009822), by a National Research Foundation of Korea (NRF) grant funded by the Korean government (MSIT) (No. 2022R1A4A2000823), and by National R&D Program through the National Research Foundation of Korea (NRF) funded by Ministry of Science and ICT (2021M3C1C3097688).

Appendix A. Supporting information

Supplementary data associated with this article can be found in the online version at doi:10.1016/j.nanoen.2022.107117.

References

[1] J. Rissman, C. Bataille, E. Masanet, N. Aden, W.R. Morrow, N. Zhou, N. Elliott, R. Dell, N. Heeren, B. Huckestein, J. Cresko, S.A. Miller, J. Roy, P. Fennell, B. Cremmins, T. Koch Blank, D. Hone, E.D. Williams, S. de la Rue du Can, B. Sisson, M. Williams, J. Katzenberger, D. Burtraw, G. Sethi, H. Ping, D. Danielson, H. Lu, T. Lorber, J. Dinkel, J. Helseth, Technologies and policies to decarbonize global industry: Review and assessment of mitigation drivers through 2070, Appl. Energy 266 (2020), 114848, https://doi.org/10.1016/j.apenergy.2020.114848.

[2] P.C. Slorach, L. Stamford, Net zero in the heating sector: technological options and environmental sustainability from now to 2050, Energy Convers. Manag. 230 (2021), 113838, https://doi.org/10.1016/j.enconman.2021.113838.

[3] S. Chu, A. Majumdar, Opportunities and challenges for a sustainable energy future, Nature 488 (2012) 294–303, https://doi.org/10.1038/nature11475.

[4] X. Zou, Y. Zhang, Noble metal-free hydrogen evolution catalysts for water splitting, Chem. Soc. Rev. 44 (2015) 5148–5180, https://doi.org/10.1039/c4cs00448e.

[5] Z. Abdin, A. Zafaranloo, A. Rafiee, W. Mérida, W. Lipiński, K.R. Khalilpour, Hydrogen as an energy vector, Renew. Sustain. Energy Rev. 120 (2020), https://doi.org/10.1016/j.rser.2019.109620.

[6] W. Liu, H. Zuo, J. Wang, Q. Xue, B. Ren, F. Yang, The production and application of hydrogen in steel industry, Int. J. Hydrog. Energy 46 (2021) 10548–10569, https://doi.org/10.1016/j.ijhydene.2020.12.123.

[7] K. Dahal, S. Brynolf, C. Xisto, J. Hansson, M. Grahn, T. Grönstedt, M. Lehtveer, Techno-economic review of alternative fuels and propulsion systems for the aviation sector, Renew. Sustain. Energy Rev. 151 (2021), https://doi.org/10.1016/j.rser.2021.111564.

[8] W.S. Chai, Y. Bao, P. Jin, G. Tang, L. Zhou, A review on ammonia, ammonia-hydrogen and ammonia-methane fuels, Renew. Sustain. Energy Rev. 147 (2021), 111254, https://doi.org/10.1016/j.rser.2021.111254.

[9] H. Xing, C. Stuart, S. Spence, H. Chen, Alternative fuel options for low carbon maritime transportation: Pathways to 2050, J. Clean. Prod. 297 (2021), 126651, https://doi.org/10.1016/j.jclepro.2021.126651.

[10] L.M. Cao, D. Lu, D.C. Zhong, T.B. Lu, Prussian blue analogues and their derived nanomaterials for electrocatalytic water splitting, Coord.Chem. Rev. 407 (2020), 213156, https://doi.org/10.1016/j.ccr.2019.213156.

[11] A. Ali, P.K. Shen, Recent progress in graphene-based nanostructured electrocatalysts for overall water splitting, Electrochem. Energy Rev. 3 (2020) 370–394, https://doi.org/10.1007/s41918-020-00066-3.

[12] Q. Hu, G. Li, Z. Han, Z. Wang, X. Huang, H. Yang, Q. Zhang, J. Liu, C. He, Recent progress in the hybrids of transition metals/carbon for electrochemical water splitting, J. Mater. Chem. A 7 (2019) 14380–14390, https://doi.org/10.1039/c9ta04163j.

[13] H. Sun, J. Dai, W. Zhou, Z. Shao, Emerging strategies for developing high-performance perovskite-based materials for electrochemical water splitting, Energy Fuels 34 (2020) 10547–10567, https://doi.org/10.1021/acs.energyfuels.0c02313.

[14] Z.P. Ifkovits, J.M. Evans, M.C. Meier, K.M. Papadantonakis, N.S. Lewis, Decoupled electrochemical water-splitting systems: a review and perspective, Energy Environ. Sci. 14 (2021) 4740–4759, https://doi.org/10.1039/d1ee01226f.

[15] N. Han, P. Liu, J. Jiang, L. Ai, Z. Shao, S. Liu, Recent advances in nanostructured metal nitrides for water splitting, J. Mater. Chem. A 6 (2018) 19912–19933, https://doi.org/10.1039/c8ta06529b.

[16] A. Indra, P.W. Menezes, I. Zaharieva, H. Dau, M. Driess, Detecting structural transformation of cobalt phosphonate to active bifunctional catalysts for electrochemical water-splitting, J. Mater. Chem. A 8 (2020) 2637–2643, https://doi.org/10.1039/c9ta09775a.

[17] V.H. Hoa, D.T. Tran, H.T. Le, N.H. Kim, J.H. Lee, Hierarchically porous nickel–cobalt phosphide nanoneedle arrays loaded micro-carbon spheres as an advanced electrocatalyst for overall water splitting application, Appl. Catal. B Environ. 253 (2019) 235–245, https://doi.org/10.1016/j.apcatb.2019.04.017.

[18] S. van Renssen, The hydrogen solution? Nat. Clim. Change 10 (2020) 799–801, https://doi.org/10.1038/s41558-020-0891-0.

[19] C. Cai, S. Han, Y. Tang, Engineering oxygen vacancies on dendrite-like IrO_2 for the oxygen evolution reaction in acidic solution, Sustain. Energy Fuels 4 (2020) 2462–2468, https://doi.org/10.1039/d0se00007h.

[20] M.R. Gao, X. Cao, Q. Gao, Y.F. Xu, Y.R. Zheng, J. Jiang, S.H. Yu, Nitrogen-doped graphene supported $CoSe_2$ nanobelt composite catalyst for efficient water oxidation, ACS Nano 8 (2014) 3970–3978, https://doi.org/10.1021/nn500880v.

[21] Y. Jiang, M. Yang, M. Qu, Y. Wang, Z. Yang, Q. Feng, X. Deng, W. Shen, M. Li, R. He, In situ confinement of Pt within three-dimensional MoO_2@porous carbon for efficient hydrogen evolution, J. Mater. Chem. A 8 (2020) 10409–10418, https://doi.org/10.1039/d0ta02507k.

[22] C. Zhang, P. Wang, W. Li, Z. Zhang, J. Zhu, Z. Pu, Y. Zhao, S. Mu, MOF-Assisted synthesis of octahedral carbon-supported PtCu nanoalloy catalysts for an efficient hydrogen evolution reaction, J. Mater. Chem. A 8 (2020) 19348–19356, https://doi.org/10.1039/d0ta06632j.

[23] Y. Li, Y. Sun, Y. Qin, W. Zhang, L. Wang, M. Luo, H. Yang, S. Guo, Recent advances on water-splitting electrocatalysis mediated by noble-metal-based nanostructured materials, Adv. Energy Mater. 10 (2020) 1–20, https://doi.org/10.1002/aenm.201903120.

[24] M.Q. Yang, J. Wang, H. Wu, G.W. Ho, Noble metal-free nanocatalysts with vacancies for electrochemical water splitting, Small 14 (2018) 1–24, https://doi.org/10.1002/smll.201703323.

[25] Z.X. Cai, H. Goou, Y. Ito, T. Tokunaga, M. Miyauchi, H. Abe, T. Fujita, Nanoporous ultra-high-entropy alloys containing fourteen elements for water splitting electrocatalysis, Chem. Sci. 12 (2021) 11306–11315, https://doi.org/10.1039/d1sc01981c.

[26] J. Dong, Y. Wang, Q. Jiang, Z.A. Nan, F.R. Fan, Z.Q. Tian, Charged droplet-driven fast formation of nickel-iron (oxy)hydroxides with rich oxygen defects for boosting overall water splitting, J. Mater. Chem. A 9 (2021) 20058–20067, https://doi.org/10.1039/d1ta05332a.

[27] B.H.R. Suryanto, Y. Wang, R.K. Hocking, W. Adamson, C. Zhao, Overall electrochemical splitting of water at the heterogeneous interface of nickel and iron oxide, Nat. Commun. 10 (2019) 1–10, https://doi.org/10.1038/s41467-019-13415-8.

[28] J. Hwang, R.R. Rao, L. Giordano, Y. Katayama, Y. Yu, Y. Shao-Horn, Perovskites in catalysis and electrocatalysis, Science 358 (2017) 751–756, https://doi.org/10.1126/science.aam7092.

[29] Y. Wang, B. Kong, D. Zhao, H. Wang, C. Selomulya, Strategies for developing transition metal phosphides as heterogeneous electrocatalysts for water splitting, Nano Today 15 (2017) 26–55, https://doi.org/10.1016/j.nantod.2017.06.006.

[30] X. Peng, Y. Yan, X. Jin, C. Huang, W. Jin, B. Gao, P.K. Chu, Recent advance and prospectives of electrocatalysts based on transition metal selenides for efficient water splitting, Nano Energy 78 (2020), 105234, https://doi.org/10.1016/j.nanoen.2020.105234.

[31] M. Wang, L. Zhang, Y. He, H. Zhu, Recent advances in transition-metal-sulfide-based bifunctional electrocatalysts for overall water splitting, J. Mater. Chem. A 9 (2021) 5320–5363, https://doi.org/10.1039/d0ta12152e.

[32] Y.H. Budnikova, Recent advances in metal-organic frameworks for electrocatalytic hydrogen evolution and overall water splitting reactions, Dalton Trans. 49 (2020) 12483–12502, https://doi.org/10.1039/d0dt01741h.

[33] Z. Wei, X. Hu, S. Ning, X. Kang, S. Chen, Supported heterostructured MoC/Mo_2C nanoribbons and nanoflowers as highly active electrocatalysts for hydrogen evolution reaction, ACS Sustain. Chem. Eng. 7 (2019) 8458–8465, https://doi.org/10.1021/acssuschemeng.9b00210.

[34] P.M. Bodhankar, P.B. Sarawade, G. Singh, A. Vinu, D.S. Dhawale, Recent advances in highly active nanostructured NiFe LDH catalyst for electrochemical water splitting, J. Mater. Chem. A 9 (2021) 3180–3208, https://doi.org/10.1039/d0ta10712c.

[35] H. Su, S. Song, S. Li, Y. Gao, L. Ge, W. Song, T. Ma, J. Liu, High-valent bimetal Ni_3S_2/Co_3S_4 induced by Cu doping for bifunctional electrocatalytic water splitting, Appl. Catal. B Environ. 293 (2021), 120225, https://doi.org/10.1016/j.apcatb.2021.120225.

[36] B. Zhang, Y. Zheng, T. Ma, C. Yang, Y. Peng, Z. Zhou, M. Zhou, S. Li, Y. Wang, C. Cheng, Designing MOF nanoarchitectures for electrochemical water splitting, Adv. Mater. 33 (2021), 2006042, https://doi.org/10.1002/adma.202006042.

[37] G. Janani, S. Surendran, H. Choi, M.K. Han, U. Sim, In situ grown $CoMn_2O_4$ 3D-tetragons on carbon cloth: flexible electrodes for efficient rechargeable zinc–air battery powered water splitting systems, Small 2103613 (2021) 1–16, https://doi.org/10.1002/smll.202103613.

[38] J.T. Mefford, X. Rong, A.M. Abakumov, W.G. Hardin, S. Dai, A.M. Kolpak, K. P. Johnston, K.J. Stevenson, Water electrolysis on $La_{1-x}Sr_xCoO_{3-\delta}$ perovskite electrocatalysts, Nat. Commun. 7 (2016), https://doi.org/10.1038/ncomms11053.

[39] J. Suntivich, K.J. May, H.A. Gasteiger, J.B. Goodenough, Y. Shao-horn, F. Calle-vallejo, A.D. Oscar, M.J. Kolb, M.T.M. Koper, J. Suntivich, K.J. May, H. A. Gasteiger, J.B. Goodenough, Y. Shao-horn, A perovskite oxide optimized for molecular orbital principles, Science 334 (2011) 2010–2012. ⟨http://www.sciencemag.org/cgi/doi/10.1126/science.1212858⟩.

[40] J. Dai, Y. Zhu, H.A. Tahini, Q. Lin, Y. Chen, D. Guan, C. Zhou, Z. Hu, H.J. Lin, T. S. Chan, C. Te Chen, S.C. Smith, H. Wang, W. Zhou, Z. Shao, Single-phase perovskite oxide with super-exchange induced atomic-scale synergistic active centers enables ultrafast hydrogen evolution, Nat. Commun. 11 (2020) 1–10, https://doi.org/10.1038/s41467-020-19433-1.

[41] N.K. Oh, C. Kim, J. Lee, O. Kwon, Y. Choi, G.Y. Jung, H.Y. Lim, S.K. Kwak, G. Kim, H. Park, In-situ local phase-transitioned $MoSe_2$ in $La_{0.5}Sr_{0.5}CoO_{3-\delta}$ heterostructure and stable overall water electrolysis over 1000 h, Nat. Commun. 10 (2019) 1–12, https://doi.org/10.1038/s41467-019-09339-y.

[42] D. Zheng, L. Yu, W. Liu, X. Dai, X. Niu, W. Fu, W. Shi, F. Wu, X. Cao, Structural advantages and enhancement strategies of heterostructure water-splitting electrocatalysts, Cell Rep. Phys. Sci. 2 (2021), 100443, https://doi.org/10.1016/j.xcrp.2021.100443.

[43] N.K. Oh, J. Seo, S. Lee, H.J. Kim, U. Kim, J. Lee, Y.K. Han, H. Park, Highly efficient and robust noble-metal free bifunctional water electrolysis catalyst achieved via complementary charge transfer, Nat. Commun. 12 (2021) 1–12, https://doi.org/10.1038/s41467-021-24829-8.

[44] G.A.M. Hutton, B.C.M. Martindale, E. Reisner, Carbon dots as photosensitisers for solar-driven catalysis, Chem. Soc. Rev. 46 (2017) 6111–6123, https://doi.org/10.1039/c7cs00235a.

[45] Y. Yan, J. Gong, J. Chen, Z. Zeng, W. Huang, K. Pu, J. Liu, P. Chen, Recent advances on graphene quantum dots: from chemistry and physics to applications, Adv. Mater. 31 (2019) 1–22, https://doi.org/10.1002/adma.201808283.

[46] S. Yang, J. Sun, X. Li, W. Zhou, Z. Wang, P. He, G. Ding, X. Xie, Z. Kang, M. Jiang, Large-scale fabrication of heavy doped carbon quantum dots with tunable-photoluminescence and sensitive fluorescence detection, J. Mater. Chem. A 2 (2014) 8660–8667, https://doi.org/10.1039/c4ta00860j.

[47] Y. Du, S. Guo, Chemically doped fluorescent carbon and graphene quantum dots for bioimaging, sensor, catalytic and photoelectronic applications, Nanoscale 8 (2016) 2532–2543, https://doi.org/10.1039/c5nr07579c.

[48] Y. Song, S. Chen, Graphene quantum-dot-supported platinum nanoparticles: Defect-mediated electrocatalytic activity in oxygen reduction, ACS Appl. Mater. Interfaces 6 (2014) 14050–14060, https://doi.org/10.1021/am503388z.

[49] B. Ma, R.D. Rodriguez, A. Ruban, S. Pavlov, E. Sheremet, The correlation between electrical conductivity and second-order Raman modes of laser-reduced graphene oxide, Phys. Chem. Chem. Phys. 21 (2019) 10125–10134, https://doi.org/10.1039/c9cp00093c.

[50] M. Zhao, J. Zhang, H. Xiao, T. Hu, J. Jia, H. Wu, Facile: In situ synthesis of a carbon quantum dot/graphene heterostructure as an efficient metal-free electrocatalyst for overall water splitting, Chem. Commun. 55 (2019) 1635–1638, https://doi.org/10.1039/c8cc09368g.

[51] S. Chen, G. He, Y. Song, K. Liu, A. Walter, S. Chen, Oxygen reduction catalyzed by platinum nanoparticles supported on graphene quantum dots, ACS Catal. 3 (2013) 831–838, https://doi.org/10.1021/cs400114s.

[52] H. Jin, H. Huang, Y. He, X. Feng, S. Wang, L. Dai, J. Wang, Graphene quantum dots supported by graphene nanoribbons with ultrahigh electrocatalytic performance for oxygen reduction, J. Am. Chem. Soc. 137 (2015) 7588–7591, https://doi.org/10.1021/jacs.5b03799.

[53] J. Heising, M.G. Kanatzidis, Exfoliated and restacked MoS_2 and WS_2: Ionic or neutral species? Encapsulation and ordering of hard electropositive cations, J. Am. Chem. Soc. 121 (1999) 11720–11732, https://doi.org/10.1021/ja991644d.

[54] J.A. Wilson, F.J. Di Salvo, S. Mahajan, Charge-density waves and superlattices in the metallic layered transition metal dichalcogenides, Adv. Phys. 24 (1975) 117–201, https://doi.org/10.1080/00018737500101391.

[55] S. Deng, Y. Zhong, Y. Zeng, Y. Wang, Z. Yao, F. Yang, S. Lin, X. Wang, X. Lu, X. Xia, J. Tu, Directional construction of vertical nitrogen-doped ^1T–^2H $MoSe_2$/graphene shell/core nanoflake arrays for efficient hydrogen evolution reaction, Adv. Mater. 29 (2017) 1–8, https://doi.org/10.1002/adma.201700748.

[56] U. Gupta, B.S. Naidu, U. Maitra, A. Singh, S.N. Shirodkar, U.V. Waghmare, C.N. R. Rao, Characterization of few-layer 1T-$MoSe_2$ and its superior performance in the visible-light induced hydrogen evolution reaction, APL Mater. 2 (2014), https://doi.org/10.1063/1.4892976.

[57] S. Wang, A. Lu, C.J. Zhong, Hydrogen production from water electrolysis: role of catalysts, Nano Converg. 8 (2021), https://doi.org/10.1186/s40580-021-00254-x.

[58] J.J. Lv, J. Zhao, H. Fang, L.P. Jiang, L.L. Li, J. Ma, J.J. Zhu, Incorporating nitrogen-doped graphene quantum dots and Ni_3S_2 nanosheets: a synergistic electrocatalyst with highly enhanced activity for overall water splitting, Small 13 (2017) 1–10, https://doi.org/10.1002/smll.201700264.

[59] H. Tang, K. Dou, C.C. Kaun, Q. Kuang, S. Yang, $MoSe_2$ nanosheets and their graphene hybrids: Synthesis, characterization and hydrogen evolution reaction studies, J. Mater. Chem. A 2 (2014) 360–364, https://doi.org/10.1039/c3ta13584e.

[60] N.N. Han, S.W. Luo, C.W. Deng, S. Zhu, Q.J. Xu, Y.L. Min, Defect-rich $FeN_{0.023}$/Mo_2C heterostructure as a highly efficient bifunctional catalyst for overall water-splitting, ACS Appl. Mater. Interfaces 13 (2021) 8306–8314, https://doi.org/10.1021/acsami.0c19839.

[61] Q. Wang, L. Ma, NO oxidative activity of mesoporous $LaMnO_3$ and $LaCoO_3$ perovskite nanoparticles by facile molten-salt synthesis, New J. Chem. 43 (2019) 2974–2980, https://doi.org/10.1039/c8nj04590a.

[62] Z. Wang, Y. You, J. Yuan, Y.X. Yin, Y.T. Li, S. Xin, D. Zhang, Nickel-doped $La_{0.8}Sr_{0.2}Mn_{1-x}Ni_xO_3$ nanoparticles containing abundant oxygen vacancies as an optimized bifunctional catalyst for oxygen cathode in rechargeable lithium-air batteries, ACS Appl. Mater. Interfaces 8 (2016) 6520–6528, https://doi.org/10.1021/acsami.6b00296.

[63] Y. Han, Y.G. Wang, W. Chen, R. Xu, L. Zheng, J. Zhang, J. Luo, R.A. Shen, Y. Zhu, W.C. Cheong, C. Chen, Q. Peng, D. Wang, Y. Li, Hollow N-doped carbon spheres

with isolated cobalt single atomic sites: superior electrocatalysts for oxygen reduction, J. Am. Chem. Soc. 139 (2017) 17269–17272, https://doi.org/10.1021/jacs.7b10194.
[64] L. Bai, C.-S. Hsu, D.T.L. Alexander, H.M. Chen, X. Hu, Double-atom catalysts as a molecular platform for heterogeneous oxygen evolution electrocatalysis, Nat. Energy (2021), https://doi.org/10.1038/s41560-021-00925-3.
[65] M.J. Kim, S. Kim, D.H. Song, S.K. Oh, K.J. Chang, E.A. Cho, Promotion of electrochemical oxygen evolution reaction by chemical coupling of cobalt to molybdenum carbide, Appl. Catal. B Environ. 227 (2018) 340–348, https://doi.org/10.1016/j.apcatb.2018.01.051.
[66] M.J. Kim, S. Kim, D.H. Song, S.K. Oh, K.J. Chang, E.A. Cho, Promotion of electrochemical oxygen evolution reaction by chemical coupling of cobalt to molybdenum carbide, Appl. Catal. B Environ. 227 (2018) 340–348, https://doi.org/10.1016/j.apcatb.2018.01.051.
[67] Y. Liu, C. Ma, Q. Zhang, W. Wang, P. Pan, L. Gu, D. Xu, J. Bao, Z. Dai, 2D electron gas and oxygen vacancy induced high oxygen evolution performances for advanced Co_3O_4/CeO_2 nanohybrids, Adv. Mater. 31 (2019) 1–9, https://doi.org/10.1002/adma.201900062.
[68] M. Gu, X. Deng, M. Lin, H. Wang, A. Gao, X. Huang, X. Zhang, Ultrathin NiCo bimetallic molybdate nanosheets coated CuO_x nanotubes: heterostructure and bimetallic synergistic optimization of the active site for highly efficient overall water splitting, Adv. Energy Mater. 11 (2021) 1–10, https://doi.org/10.1002/aenm.202102361.
[69] S. Zhao, C. Li, J. Liu, N. Liu, S. Qiao, Y. Han, H. Huang, Y. Liu, Z. Kang, Carbon quantum dots/SnO_2-Co_3O_4 composite for highly efficient electrochemical water oxidation, Carbon 92 (2015) 64–73, https://doi.org/10.1016/j.carbon.2015.03.002.
[70] J. Liu, J. Wang, B. Zhang, Y. Ruan, H. Wan, X. Ji, K. Xu, D. Zha, L. Miao, J. Jiang, Mutually beneficial Co_3O_4@MoS_2 heterostructures as a highly efficient bifunctional catalyst for electrochemical overall water splitting, J. Mater. Chem. A 6 (2018) 2067–2072, https://doi.org/10.1039/c7ta10048e.
[71] N. Li, J. Wu, Y. Lu, Z. Zhao, H. Zhang, X. Li, Y.Z. Zheng, X. Tao, Stable multiphasic 1T/2H $MoSe_2$ nanosheets integrated with 1D sulfide semiconductor for drastically enhanced visible-light photocatalytic hydrogen evolution, Appl. Catal. B Environ. 238 (2018) 27–37, https://doi.org/10.1016/j.apcatb.2018.07.002.
[72] T. Sun, Q. Wu, R. Che, Y. Bu, Y. Jiang, Y. Li, L. Yang, X. Wang, Z. Hu, Alloyed Co-Mo nitride as high-performance electrocatalyst for oxygen reduction in acidic medium, ACS Catal. 5 (2015) 1857–1862, https://doi.org/10.1021/cs502029h.
[73] D. Voiry, M. Salehi, R. Silva, T. Fujita, M. Chen, T. Asefa, V.B. Shenoy, G. Eda, M. Chhowalla, Conducting MoS_2 nanosheets as catalysts for hydrogen evolution reaction, Nano Lett. 13 (2013) 6222–6227, https://doi.org/10.1021/nl403661s.
[74] Y. Li, Y. Zhao, H. Cheng, Y. Hu, G. Shi, L. Dai, L. Qu, Nitrogen-doped graphene quantum dots with oxygen-rich functional groups, J. Am. Chem. Soc. 134 (2012) 15–18, https://doi.org/10.1021/ja206030c.
[75] R.J. Koch, M. Weser, W. Zhao, F. Viñes, K. Gotterbarm, S.M. Kozlov, O. Höfert, M. Ostler, C. Papp, J. Gebhardt, H.P. Steinrück, A. Görling, T. Seyller, Growth and electronic structure of nitrogen-doped graphene on Ni(111), Phys. Rev. B Condens. Matter Mater. Phys. 86 (2012), https://doi.org/10.1103/PhysRevB.86.075401.
[76] F. Orlando, P. Lacovig, M. Dalmiglio, A. Baraldi, R. Larciprete, S. Lizzit, Synthesis of nitrogen-doped epitaxial graphene via plasma-assisted method: Role of the graphene-substrate interaction, Surf. Sci. 643 (2016) 214–221, https://doi.org/10.1016/j.susc.2015.06.017.
[77] M. Ghiyasiyan-Arani, M. Salavati-Niasari, Comparative study on electrochemical hydrogen storage of nanocomposites based on S or N doped graphene quantum dots and nanostructured titanium niobate, J. Alloy. Compd. 899 (2022), 163379, https://doi.org/10.1016/j.jallcom.2021.163379.
[78] S. Yang, W. Jia, Y. Wang, W. Zhang, X. Yuan, Hydroxylated graphene: a promising reinforcing nanofiller for nanoengineered cement composites, ACS Omega 6 (2021) 30465–30477, https://doi.org/10.1021/acsomega.1c03844.
[79] X. Wang, X. Li, L. Zhang, Y. Yoon, P.K. Weber, H. Wang, J. Guo, H. Dai, N-doping of graphene through electrothermal reactions with ammonia, Science 324 (2009) 768–771, https://doi.org/10.1126/science.1170335.
[80] J. Xie, K. Huang, X. Yu, Z. Yang, K. Xiao, Y. Qiang, X. Zhu, L. Xu, P. Wang, C. Cui, D. Yang, Enhanced electronic properties of SnO_2 via electron transfer from graphene quantum dots for efficient perovskite solar cells, ACS Nano 11 (2017) 9176–9182, https://doi.org/10.1021/acsnano.7b04070.
[81] D. Usachov, O. Vilkov, A. Grüneis, D. Haberer, A. Fedorov, V.K. Adamchuk, A. B. Preobrajenski, P. Dudin, A. Barinov, M. Oehzelt, C. Laubschat, D.V. Vyalikh, Nitrogen-doped graphene: efficient growth, structure, and electronic properties, Nano Lett. 11 (2011) 5401–5407, https://doi.org/10.1021/nl2031037.
[82] T. Schiros, D. Nordlund, L. Pálová, D. Prezzi, L. Zhao, K.S. Kim, U. Wurstbauer, C. Gutiérrez, D. Delongchamp, C. Jaye, D. Fischer, H. Ogasawara, L.G. M. Pettersson, D.R. Reichman, P. Kim, M.S. Hybertsen, A.N. Pasupathy, Connecting dopant bond type with electronic structure in n-doped graphene, Nano Lett. 12 (2012) 4025–4031, https://doi.org/10.1021/nl301409h.
[83] H. Kozuka, H. Yamada, T. Hishida, K. Yamagiwa, K. Ohbayashi, K. Koumoto, Electronic transport properties of the perovskite-type oxides $La_{1-x}Sr_xCoO_{3\pm\delta}$, J. Mater. Chem. 22 (2012) 20217–20222, https://doi.org/10.1039/c2jm34613c.
[84] D.S. Schulman, A.J. Arnold, S. Das, Contact engineering for 2D materials and devices, Chem. Soc. Rev. 47 (2018) 3037–3058, https://doi.org/10.1039/c7cs00828g.
[85] C. Hu, M. Li, J. Qiu, Y.P. Sun, Design and fabrication of carbon dots for energy conversion and storage, Chem. Soc. Rev. 48 (2019) 2315–2337, https://doi.org/10.1039/c8cs00750k.

Chen Tian Cao is a Master candidate in the School of Advanced Materials Science and Engineering at Sungkyunkwan University (SKKU). Her current research mainly focused on bifunctional electrocatalysts for oxygen evolution reaction and hydrogen evolution reaction.

Sun-Woo Kim is a Ph.D. candidate under the supervision of Prof. Jeong Min Baik at School of Advanced Materials Science and Engineering at Sungkyunkwan University (SKKU). His doctoral research focuses on hybrid generator based triboelectric generators and thermoelectric generator for sustainable energy conversions.

Hee Jun Kim is a postdoctoral associate at School of Advanced Materials Science and Engineering at Sungkyunkwan University (SKKU). He received his Ph.D. from Ulsan National Institute of Science and Technology (UNIST) in School of Materials Science and Engineering in 2020. His current research mainly focused on perovskite oxide synthesis for sensing and energy applications.

Rahul Purbia is a postdoctoral associate at School of Advanced Materials Science and Engineering at Sungkyunkwan University (SKKU). He received his Ph.D. from National Institute of Technology in Department of Chemical engineering in 2019. His current research mainly focused on mesoporous materials for sensing and energy harvesting.

Sang Heon Kim is a combined Master/Ph.D candidate in School of Advanced Materials Science and Engineering at Sungkyunkwan University (SKKU). His current research mainly focused on bifunctional electrocatalysts for oxygen evolution reaction and hydrogen evolution reaction.

Dokyoung Kim is an Assistant Professor in department of Biomedical Science, Kyung Hee University. He received his Ph. D. from the Department of Chemistry at POSTECH (Pohang University of Science and Technology) in 2014. After a postdoctoral stay at the University of California, San Diego (2015–2017), he started his independent career at Kyung Hee University, College of Medicine, Seoul. He has been interested in biomedical applications of fluorescent materials and nanomaterials.

Prof. Kyoung Jin Choi is now Associate Professor in School of Materials Science and Engineering, Ulsan National Institute of Science and Technology (UNIST). He received his Ph.D. from Pohang University in Department of Materials Science and Engineering in 2001. His recent research interest is focused on thermoelectric energy harvesters and photovoltaic devices such as tandem cells, organic/inorganic hybrid cells, and TMDC-based ones.

Dr. Hyesung Park is an Associate Professor in School of Energy and Chemical Engineering at Ulsan National Institute of Science and Technology (UNIST), South Korea. He received his M. S. and Ph.D. degrees in Mechanical Engineering and Electrical Engineering and Computer Science from Massachusetts Institute of Technology (MIT) in 2007 and 2012. He was a postdoctoral associate at MIT from 2012 to 2013 and postdoctoral fellow at Northwestern University in 2014. His research interests focus on synthesis of low-dimensional materials and their applications into functional devices.

Dr. Jeong Min Baik is Professor in School of Advanced Materials Science and Engineering at Sungkyunkwan University (SKKU). He received his M.S. and Ph.D. from Pohang University in Department of Materials Science and Engineering in 2001 and 2006. His recent research interest is focused on the synthesis of nanomaterials and nanostructures such as nanoparticles, nanowires, nanolayers, and nanopores for the applications of Energy-Conversion Devices and Nano-photonic Devices. Particular interests are concerned with the development of Piezoelectric/Triboelectric Nanogenerators and Artificial Photosynthesis.